

Chapter 1

Results and analysis

In this chapter we will showcase a series of results from the MEQSILHOUETTE simulator in order to demonstrate it's capabilities and predictions.

1.1 Canonical simulations

Author's note: This section draws largely from the work of Blecher et al. [2016].

ISM variability and substructure

We remind the reader of the reproduction of the ISM-induced closure phase uncertainty result [Ortiz-León et al., 2016], shown in Fig. ???. To obtain this result we simulated 50 observations, each with an independent realisation of the ISM scattering screen. The success of the reproduction verifies a large section of the simulation software, including I/O, the interferometric and the ISM modules.

Following the discussion on the ISM theory (section ??), we compare predictions of the ensemble-averaging regime, which consists of only a Gaussian convolution, and the average regime, which includes the presence of stochastic substructure. Note that the ensemble-average is invariant with time and

would not bias the closure phase of a point-symmetric source.

“We present the results of a simulated observation of 10 minutes duration at 14:00 UTC on four consecutive days in Fig. 1.1. To compare to published observations, we use the three-station EHT array consisting of the Submillimeter Telescope (SMT) in Arizona, the Combined Array for Research in Millimeter-wave Astronomy (CARMA) in California and the James Clerk Maxwell Telescope (JCMT) on Mauna Kea, Hawaii. The relative transverse velocity between the observer and scattering screen is set to 50 km s^{-1} to be consistent with Ortiz-León et al. [2016]. The source is a circular Gaussian with a $\text{FHWM} = 40 \mu\text{-arcsec}$, approximately the angular distance that a scattering screen would travel over ~ 4 days. The source size has been chosen such that it is consistent with the latest estimate of the size of Sgr A* at 230 GHz [Fish et al., 2011]. Closure quantities are model dependent and calculated as specified in Rogers et al. [1995], where the thermal noise was added based on the system equivalent flux density (SEFD) table in [Lu et al., 2014].

Fig. 1.1 provides an example of closure phase and flux variability over a 4 day period using a static source. Accurate simulation of the ISM-induced closure phase variation is essential in order to make any inference on asymmetric, event-horizon scale structure [e.g. Fish et al., 2016, Ortiz-León et al., 2016]. This will become even more important as the EHT sensitivity increases by an order of magnitude in the near future when [phased ALMA is included in the array.]” [Blecher et al., 2016]

This simulation clearly shows how the longest baselines are more sensitive to the refractive substructure, which in turn strengthens the challenge of imaging compact features and/or fine structure like the BH shadow.

Recalling the variability associated with Sgr A* (section ??), if the source has intrinsic spatial variability, e.g. an orbiting hotspot model [Doeleman et al., 2009] or jet shocks, this will increase ISM variability as the relative motion between source, screen and observer is increased [Blecher et al., 2016]. Although an orbiting plasma blob might be torn apart on sub-orbit timescales by differential rotation and the non-linear shear of the Magneto-Rotational Instability [(MRI) ?], this scenario becomes more of a physical possibility when resonant orbits are considered [?]. A resonant orbit occurs when the ratio of characteristic radial ω_r and longitudinal frequencies ω_θ is a rational number $\omega_r/\omega_\theta = n/m$, where $n, m \in \mathbb{N}$. A hotspot in such an orbit could be stable against differential rotation and associated shearing. In the case of Sgr A*, the 1/2 and 2/3 resonances have length scales of 41 and 55 $\mu\text{-arcsec}$ respectively for a Schwarzschild BH [?], which is observable with the EHT. Also note that these resonant length scales are greater than $r_{\text{ref}} \sim 10 \mu\text{-arcsec}$ and so the orbit would traverse independent refractive substructure fluctuations. This is relevant to methods like that demonstrated in Doeleman et al. [2009] which rely on periodic closure phases. The periodic signal would exist (albeit altered by the ISM) but only on timescales less than t_{ref} , assuming the orbiting body is unresolved.

Finally, we note that the ISM is polarisation invariant, hence the variability of polarisation ratios will not be biased by ISM scattering. Methods which use polarisation ratios [e.g. Johnson et al., 2014] allows for valuable insight into how the source variability and ISM variability could be separated.

Atmospheric transmission and scattering

As described in section ??, the implementation of the tropospheric module is separated into mean and turbulent components. For the mean atmosphere, we simulate opacity, sky brightness temperature and time delay as a function of site weather, elevation angle and frequency. The most important climate parameters are precipitable water vapour column depth (PWV), ground tem-

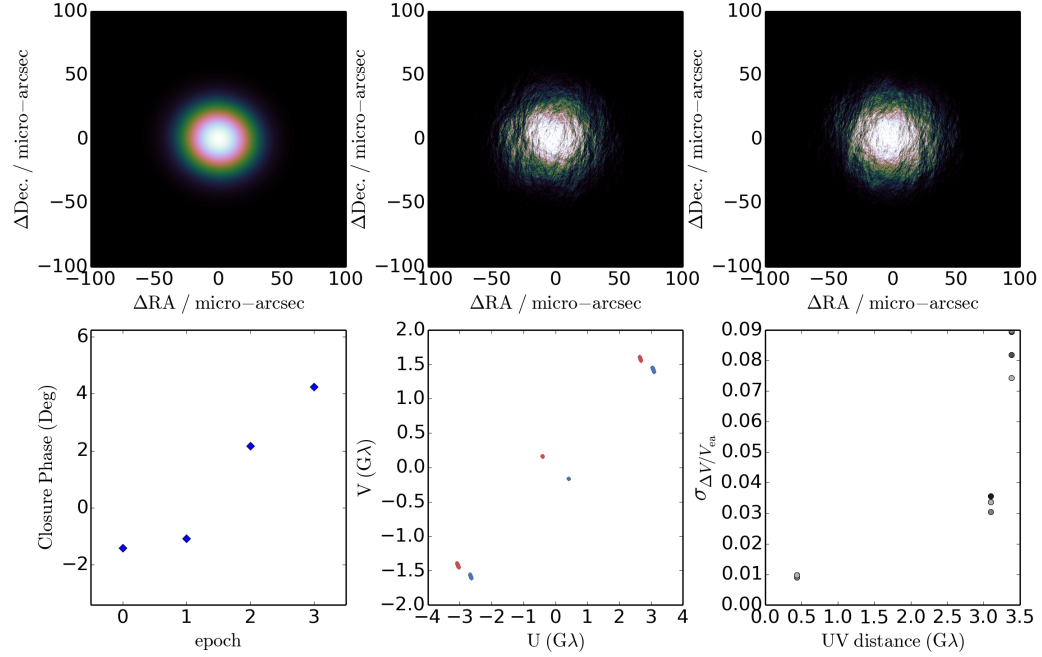


Figure 1.1: “An example simulation of ISM scattering towards Sgr A \star , observed with SMT-JCMT-CARMA. The top panel, left to right, shows the original FWHM = 40 μ -arcsec Gaussian (**top left**), the simulated ISM scattered image on the first night (**top middle**) and last night (**top right**) of the observation, respectively. The bottom panel, left to right, shows the evolution of the 10 minute-averaged closure phase with epoch (**bottom left**), uv-tracks for each night (**bottom middle**) and the RMS fractional visibility amplitude differences $\sigma_{\Delta V}/V_{ea}$ as a function of *uv*-distance (**bottom right**). $\Delta V = (|V_a| - |V_{ea}|)$, where $|V_a|$ and $|V_{ea}|$ are the simulated average and ensemble average visibility amplitudes respectively. Variations from the ensemble-average flux on the shortest baselines reveal total flux modulation while flux variations on longer baselines and non-zero closure phases track the fluctuations in substructure.” (Image and caption reproduced from Blecher et al. [2016])

perature and ground pressure. The turbulent module simulates Gaussian fluctuations in the time delay \tilde{t} arriving at each station, where $\sigma(\tilde{t})$ is based on Kolmogorov turbulence on a two-dimensional scattering screen.

The first atmospheric result we present are mean opacities and sky brightness temperatures for ALMA, the Submillimeter Array (SMA) and the South Pole Telescope (SPT) at 230 GHz, shown in Fig. 1.2. These sites were chosen as they are all considered excellent sites for sub-mm astronomy and form an essential part of the EHT. The PWV ranges used were taken from the 25th and 75th percentile data shown in Lane [1998] and is in good agreement with the measured opacities therein.

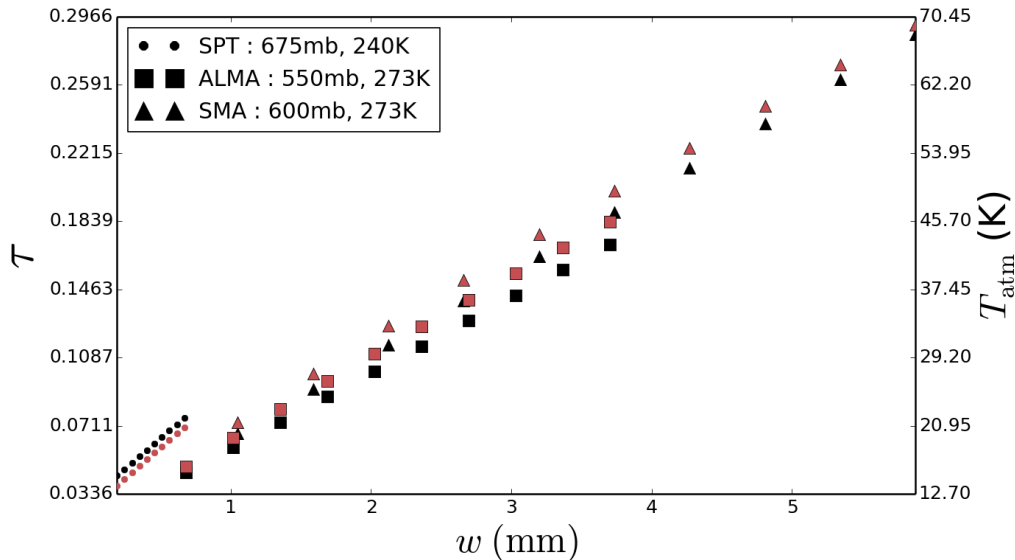


Figure 1.2: “Simulated mean opacity (black) and sky brightness temperature (red) at $\nu = 230$ GHz for three typical ground pressures and temperatures over a typical PWV range [Lane, 1998] which approximately represent the sites of SPT (dots), ALMA (squares) and SMA (triangles). The legend shows the estimated input ground (pressure, temperature) parameters for each site.” (Image and caption reproduced from Blecher et al. [2016])

Immediately apparent is that the opacity and sky brightness temperature both exhibit linear relationships with respect to PWV content. Furthermore, opacity and sky brightness temperature are proportional to ground pressure and inversely proportional to the ground temperature [?]. It is also clear that SPT has far less opacity, and a lower sky brightness temperature than

ALMA and the SMA which are fairly similar. A comparison of the thermal receiver temperatures for the three sites (ALMA \sim 262 K, SMA \sim 327 K, SPT \sim 255 K) reveals that for the thermal noise contribution from the receiver is approximately an order of magnitude higher than sky brightness temperature.

Of vital importance to an interferometric site is atmospheric stability. An example of the effects of atmospheric transmission and scattering on the time delay \tilde{t} at 230 GHz is shown as a function of observation time in Fig. 1.3. Canonical values (see caption) were used for the weather parameters. It is apparent that the turbulent component is typically 3-4 orders of magnitude lower than the mean delay, even though the coherence time is on the order of seconds.

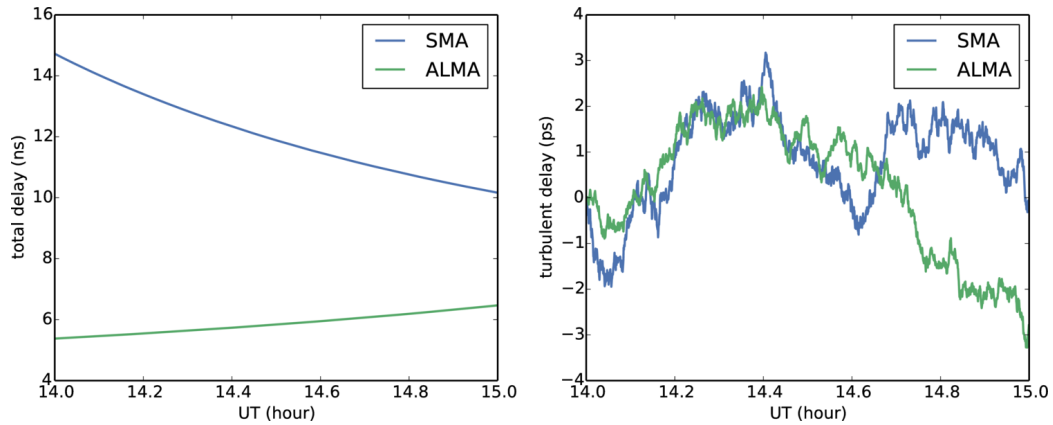


Figure 1.3: “Simulation of the total delay (left) and the turbulent atmospheric delay (right) for SMA (blue) and ALMA (green) sites towards Sgr A*. Ground pressures and temperatures are the same as Fig. 1.2, precipitable water vapour above each station is set to $w = 2$ mm, and the instantaneous zenith coherence time is set $T_0 = 10$ s for both stations. Note that all tropospheric parameters are, however, independently set. The conversion from time delay to phase at 230 GHz is 1 rad = 0.7 ps.” (Image and caption reproduced from Blecher et al. [2016])

“We now investigate the effect of the tropospheric module on

image quality for various levels of calibration accuracy. We simulate the simple scenario of a sky model that consists of a 2.4 Jy point source at the phase centre, which is an approximate EHT-measured flux density of Sgr A* at 230 GHz. We assume a zenith phase coherence time of $t_0 = 10$ s above each station (however, each stations PWV can be independently simulated). We approximate the effect of imperfect calibration by adding a small fraction of the turbulent phase noise. For this example, we do not include the mean delay component, assuming it to be perfectly corrected for during the calibration. Imaging [is performed] using the two dimensional inverse fast Fourier transform”

[Blecher et al., 2016]

Analysis of the images reveal increasing attenuation in the original peak, central flux due to the simulated residual calibration errors. In the calibration procedure, station gains cannot be solved for on arbitrarily short intervals as adequate SNR is needed to fringe-fit/self-calibrated. Aside from the fact that solutions are imperfect, within a given solution interval, there will also be a degree of uncalibrated turbulence-induced phase fluctuations.

Specifically, the flux of central peak component is reduced to 76.5% (attenuation only - not shown in plot), 75.1% (1% turbulence), 65.5% (2% turbulence) and 40.5% (3% turbulence). In the case of 3% turbulence, the lower imaging artifact becomes brighter than the original source (44.5%).

Furthermore, there are slight offsets in the peak central flux from the original source position as shown by progressive movement away from the black crosshairs. This shift becomes $5.6 \mu\text{-arcsec}$ at 3% turbulence.

The residual calibration errors also distort the interferometric artifacts, which result from inadequate sampling of the Fourier domain before imaging. This could cause a breakdown in image-plane deconvolution and source finding algorithms as the sidelobes are difficult to subtract and interferometric artefacts are difficult to distinguish from source structure, in turn further

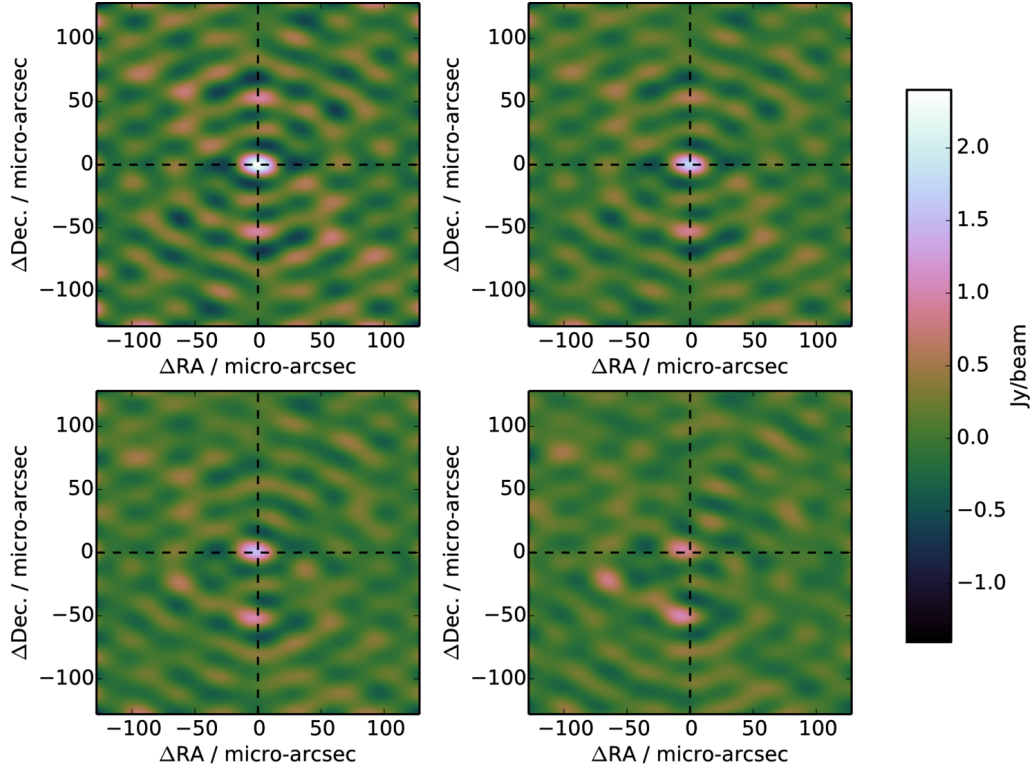


Figure 1.4: “The effect of residual troposphere phase noise on interferometric images of a point source observed for 12 hours at 230 GHz with 4 GHz bandwidth with the following array : SPT, ALMA, SMA, SMT, LMT and JCMT, assuming the same SEFDs as Lu et al. [2014] and an elevation limit of 15° . For simplicity the weather parameters at each station were set to: coherence time $t_0 = 10$ sec; PWV depth $w = 1$ mm; ground pressure $P = 600$ mb; ground temperature $T = 273$ K. **Top left:** interferometric map with thermal noise only. **Top right:** atmospheric attenuation and sky noise (due to non-zero opacity) with 1% of the turbulent phase noise added. **Bottom left:** as previous but with 3% of turbulent phase contribution. **Bottom right:** as previous but with 6% turbulent phase contribution. The fractional turbulent phase contributions are illustrative of the effect of fringe-fitting errors. The black crosshairs indicate the original source position. ”(Image and caption reproduced from Blecher et al. [2016])

weakening the ability of algorithms which use this procedure to extract, with high fidelity, the BH shadow feature.

There was no evidence of blurring or a loss of resolution. Blurring can result if the decoherence is considered as a function of baseline length, longer baseline would be more decoherent and their visibilities are effectively down-weighted. For the EHT, as different stations experience independent different turbulent intensities, the baseline length will not be correlated with the magnitude of the decoherence. The blurring effect common to optical telescopes, known as ‘seeing’ which is induced by the overlaying of many speckled images of the source [Narayan, 1992] across the scattering disc, does not seem to occur in the interferometric process. We suspect that this is due to the cancellation of possibly this does not occur due to the negatives in the Fourier transform modes.

Pointing

“We investigate the effect of pointing errors on the 50 m (i.e. fully illuminated) Large Millimeter Array (LMT) dish configured in an eight station VLBI array. The LMT has been measured to have an absolute pointing accuracy of $\sigma_{\text{abs}} = 1 - 3 \text{ arcsec}$, where smaller offsets occur when observing sources closer to zenith, and a tracking pointing accuracy $\sigma_{\text{track}} < 1 \text{ arcsec}^1$. We investigate the observational effect of these errors through three different pointing error models which explore different instructive and plausible scenarios. The LMT has been singled out as this may well serve as a reference station for the EHT array given its sensitivity and central geographic location. The source used is a circular Gaussian of characteristic size $\Theta_{\text{src}} = 50 \mu\text{-arcsec}$, located at the phase centre. For this investigation, as long as $\Theta_{\text{src}} \ll \theta_{\text{PB}}$, the exact structure of the source is unimportant.

¹<http://www.lmtgtm.org/telescope/telescope-description/>

We approximate the LMT beam profile using an analytic WSRT beam model (equation ??) with a factor of two increase in the beam factor C to take into account the increased dish size.”

[Blecher et al., 2016]

[!! TO check C - is this fWHM for LMT or WSRT?? - also repeated in imp] where C is a constant, with value $C \approx 130 \text{ GHz}^{-1}$. Note that the power beam EE^H becomes \cos^6 , resulting in a FWHM = 6.5 arcsec at 230 GHz.

We make use of the RMS fractional visibility amplitude error $\sigma_{\Delta V/V_0}$, where V_{PE} and V_0 are the visibility amplitudes with and without pointing errors respectively, and $\Delta V = V_{\text{PE}} - V_0$. In Fig. 1.5, $\sigma_{\Delta V/V_0}$ is plotted against pointing error ρ over the range $0 \leq \rho \leq 4.5 \text{ arcsec}$.

In the first case we assume a *constant* pointing error. This simulation is meant to be instructive as to the typical amplitude error in the simplest possible scenario.

” [to be merged with the previous quotation] In this simulation, we only consider LMT pointing errors due to its narrow primary beam and potential to be used as a reference station. However, the capability to simulate independent pointing errors for each station is available. In the case of a phased array, a pointing error simulation could be used to investigate the contribution of the pointing error to a variable phasing efficiency, which can be reasonably approximated by a scalar Jones matrix.” ”

“Visibility amplitude errors due to antenna pointing error has been investigated for the 50 m LMT dish operating at 230 GHz. In Fig. 1.5, we show that pointing errors associated with frequent phase centre switching (stochastic variability) could introduce a RMS fractional amplitude error $\sigma_{\Delta V/V_0} \sim 0.1 - 0.4$ for an absolute pointing accuracy $\sigma_{\text{abs}} \sim 1 - 3 \text{ arcsec}$. In contrast, tracking errors are less problematic with $\sigma_{\Delta V/V_0} \leq 0.05$ for a tracking accuracy $\sigma_{\text{track}} < 1 \text{ arcsec}$. The case of a constant error pointing model is

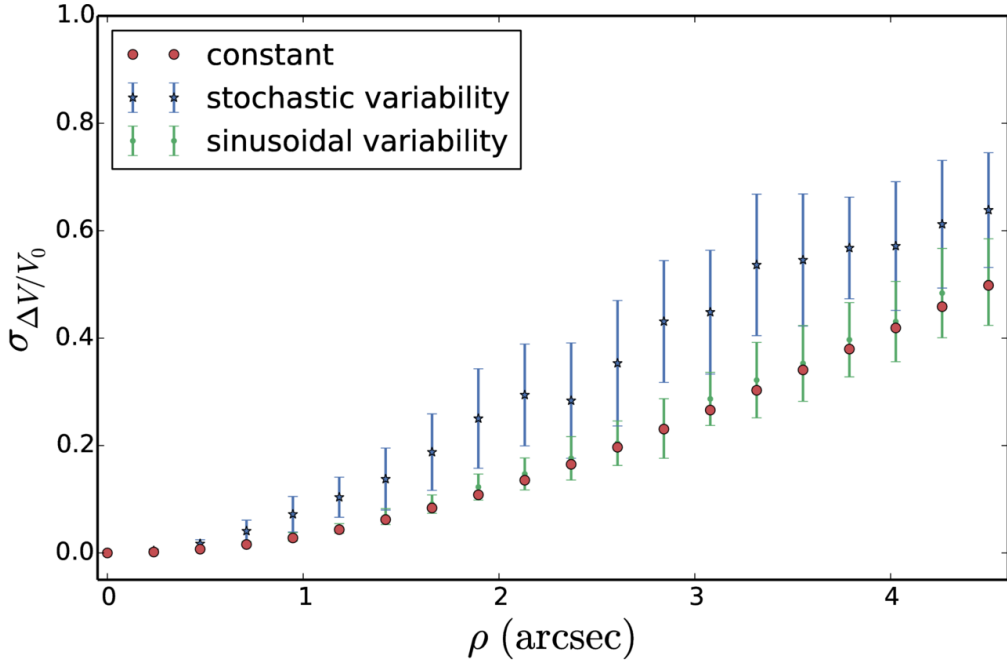


Figure 1.5: “RMS relative amplitude error induced by pointing error with the 50 m (i.e. fully illuminated) LMT antenna as a function of pointing error offset ρ at 230 GHz. We assume that these errors are degenerate or non-separable from the self-calibration/fringe-fitting model used. See text for the description of the three models used. This simulation capability enables constraints on the magnitude of pointing-induced errors given a particular pointing calibration strategy.” (Image and caption reproduced from Blecher et al. [2016])

comparable to that of the ‘slow variability’ case. If the gain error is non-separable from the calibration model used, it could be interpreted as intrinsic variability, substructure and/or increased noise. If unaccounted for, this effect has the potential to limit the dynamic range of mm-VLBI images. Further tests to constrain the pointing uncertainties of EHT stations will lead to more accurate interferometric simulations and hence the overall impact on black hole shadow parameter estimation. Here we demonstrate

the capability to incorporate a range of plausible pointing error effects into a full simulation pipeline. For future observations at 345 GHz, these effects will be even more pronounced, given the narrower primary beam.

[..]

[Blecher et al., 2016]

Bibliography

- T. Blecher, R. Deane, G. Bernardi, and O. Smirnov. MeqSilhouette : A mm-VLBI observation and signal corruption simulator. *MNRAS*, September 2016. doi: 10.1093/mnras/stw2311.
- S. S. Doeleman, V. L. Fish, A. E. Broderick, A. Loeb, and A. E. E. Rogers. Detecting Flaring Structures in Sagittarius A* with High-Frequency VLBI. *ApJ*, 695:59–74, April 2009. doi: 10.1088/0004-637X/695/1/59.
- V. L. Fish, S. S. Doeleman, C. Beaudoin, R. Blundell, D. E. Bolin, G. C. Bower, R. Chamberlin, R. Freund, P. Friberg, M. A. Gurwell, M. Honma, M. Inoue, T. P. Krichbaum, J. Lamb, D. P. Marrone, J. M. Moran, T. Oyama, R. Plambeck, R. Primiani, A. E. E. Rogers, D. L. Smythe, J. SooHoo, P. Strittmatter, R. P. J. Tilanus, M. Titus, J. Weintraub, M. Wright, D. Woody, K. H. Young, and L. M. Ziurys. 1.3 mm Wavelength VLBI of Sagittarius A*: Detection of Time-variable Emission on Event Horizon Scales. *ApJ*, 727:L36, February 2011. doi: 10.1088/2041-8205/727/2/L36.
- Vincent L. Fish, Michael D. Johnson, Sheperd S. Doeleman, Avery E. Broderick, Dimitrios Psaltis, Ru-Sen Lu, Kazunori Akiyama, Walter Alef, Juan Carlos Algaba, Keiichi Asada, Christopher Beaudoin, Alessandra Bertarini, Lindy Blackburn, Ray Blundell, Geoffrey C. Bower, Christiaan Brinkerink, Roger Cappallo, Andrew A. Chael, Richard Chamberlin, Chi-Kwan Chan, Geoffrey B. Crew, Jason Dexter, Matt Dexter, Ser-

- gio A. Dzib, Heino Falcke, Robert Freund, Per Friberg, Christopher H. Greer, Mark A. Gurwell, Paul T. P. Ho, Mareki Honma, Makoto Inoue, Tim Johannsen, Junhan Kim, Thomas P. Krichbaum, James Lamb, Jonathan León-Tavares, Abraham Loeb, Laurent Loinard, David MacMahon, Daniel P. Marrone, James M. Moran, Monika Mościbrodzka, Gisela N. Ortiz-León, Tomoaki Oyama, Feryal Özel, Richard L. Plambeck, Nicolas Pradel, Rurik A. Primiani, Alan E. E. Rogers, Katherine Rosenfeld, Helge Rottmann, Alan L. Roy, Chester Ruszczyk, Daniel L. Smythe, Jason SooHoo, Justin Spilker, Jordan Stone, Peter Strittmatter, Remo P. J. Tilanus, Michael Titus, Laura Vertatschitsch, Jan Wagner, John F. C. Wardle, Jonathan Weintraub, David Woody, Melvyn Wright, Paul Yamaguchi, André Young, Ken H. Young, J. Anton Zensus, and Lucy M. Ziurys. PERSISTENT ASYMMETRIC STRUCTURE OF SAGITTARIUS A* ON EVENT HORIZON SCALES. *ApJ*, 820(2):90, mar 2016. doi: 10.3847/0004-637x/820/2/90. URL <http://dx.doi.org/10.3847/0004-637x/820/2/90>.
- M. D. Johnson, V. L. Fish, S. S. Doeleman, A. E. Broderick, J. F. C. Wardle, and D. P. Marrone. Relative Astrometry of Compact Flaring Structures in Sgr A* with Polarimetric Very Long Baseline Interferometry. *ApJ*, 794: 150, October 2014. doi: 10.1088/0004-637X/794/2/150.
- A. P. Lane. Submillimeter Transmission at South Pole. In G. Novak and R. Landsberg, editors, *Astrophysics From Antarctica*, volume 141 of *Astronomical Society of the Pacific Conference Series*, pages 289–295, 1998.
- Ru-Sen Lu, Avery E. Broderick, Fabien Baron, John D. Monnier, Vincent L. Fish, Sheperd S. Doeleman, and Victor Pankratius. IMAGING THE SUPERMASSIVE BLACK HOLE SHADOW AND JET BASE OF M87 WITH THE EVENT HORIZON TELESCOPE. *ApJ*, 788(2):120, may 2014. doi: 10.1088/0004-637x/788/2/120. URL <http://dx.doi.org/10.1088/0004-637x/788/2/120>.

R. Narayan. The Physics of Pulsar Scintillation. *Philosophical Transactions of the Royal Society A: Mathematical Physical and Engineering Sciences*, 341(1660):151–165, oct 1992. doi: 10.1098/rsta.1992.0090. URL <http://dx.doi.org/10.1098/rsta.1992.0090>.

G. N. Ortiz-León, M. D. Johnson, S. S. Doeleman, L. Blackburn, V. L. Fish, L. Loinard, M. J. Reid, E. Castillo, A. A. Chael, A. Hernández-Gómez, D. H. Hughes, J. León-Tavares, R.-S. Lu, A. Montaña, G. Narayanan, K. Rosenfeld, D. Sánchez, F. P. Schloerb, Z.-q. Shen, H. Shiokawa, J. SooHoo, and L. Vertatschitsch. The Intrinsic Shape of Sagittarius A* at 3.5 mm Wavelength. *ApJ*, 824:40, June 2016. doi: 10.3847/0004-637X/824/1/40.

J.R. Pardo, J. Cernicharo, and E. Serabyn. Atmospheric transmission at microwaves (ATM): an improved model for millimeter/submillimeter applications. *IEEE Trans. Antennas Propagat.*, 49(12):1683–1694, 2001. doi: 10.1109/8.982447. URL <http://dx.doi.org/10.1109/8.982447>.

Alan E. E. Rogers, Sheperd S. Doeleman, and James M. Moran. Fringe detection methods for very long baseline arrays. *AJ*, 109:1391, mar 1995. doi: 10.1086/117371. URL <http://dx.doi.org/10.1086/117371>.